Tribological Behavior of NiTi Alloy Produced by Spark Plasma Sintering Method

Sneha Samal [1],*[ID], Jana Cibulková [2][ID], Radim Čtvrtlík [3,4],*, Jan Tomáštík [3,4][ID], Lukáš Václavek [3,4], Jaromír Kopeček [1][ID] and Petr Šittner [1][ID]

[1] Department of Functional Materials, FZU-Institute of Physics of the Czech Academy of Sciences, Na Slovance 1992/2, 182 21 Prague, Czech Republic; kopecek@fzu.cz (J.K.); sittner@fzu.cz (P.Š.)
[2] Central Laboratories, University of Chemistry and Technology, Prague (UCT Prague), 166 28 Prague, Czech Republic; Jana.Cibulkova@vscht.cz
[3] Joint Laboratory of Optics of Palacký University and Institute of Physics AS CR, Faculty of Science, Palacký University in Olomouc, 17 Listopadu 50a, 772 07 Olomouc, Czech Republic; tomastik@fzu.cz (J.T.); vaclavek@fzu.cz (L.V.)
[4] Joint Laboratory of Optics of Palacky University and Institute of Physics AS CR, Institute of Physics of the Czech Academy of Sciences, 17 Listopadu 50a, 772 07 Olomouc, Czech Republic
*   Correspondence: samal@fzu.cz (S.S.); ctvrtlik@fzu.cz (R.Č.); Tel.: +420-266-052-361 (S.S.)

Abstract: The tribological behaviors of NiTi alloy produced by the spark plasma sintering (SPS) method before and after annealing were investigated at various loading conditions via indentation, scratch, and wear tests. Indentation tests were performed by a pyramidal Berkovich indenter, while scratch and wear tests were carried out by a diamond Rockwell spherical indenter at room temperature. The annealing of the as-prepared samples was performed at 350, 450, and 550 °C in the ambient atmosphere. The influence of the annealing temperature on the sample behavior towards tribological study was investigated here. The results indicated that the alloy annealed at 350 °C showed a higher hardness compared to the other annealed alloys. The scratch and wear resistance of the annealed sample at 350 °C showed a better performance in comparison to the other samples under a constant load. The high wear resistance of the annealed NiTi alloy may be attributed to its metastable R-phase. The detection and evaluation of acoustic emissions during the nano/micro-tribomechanical testing proved to be a very effective way for the exploration of the durability of SPS NiTi alloys.

Keywords: NiTi alloy; annealing; indentation; wear; scratch test

1. Introduction

NiTi shape memory alloy (SMA) has been subjected to interest in the field of tribology-related applications in various areas at harsh operating conditions [1]. Due to its superior wear resistance, corrosion resistance, biocompatibility, and shape memory behavior, NiTi alloy is a very promising material in biomedical devices such as NiTi needles, wires, stents, or super-elastic arch-wires. An alternative route is developed in the area of powder metallurgy such as spark plasma sintering (SPS) for the feasible method of successful NiTi alloy fabrication [2–5]. The $Ni_{50}Ti_{50}$ alloy possesses a unique shape memory effect and transformation pseudoelasticity. The pseudoelastic strain can reach up to 8–20% by two orders of magnitude larger than ordinary elasticity [6,7]. NiTi alloys exhibit good wear resistance in sliding wear and cavitation erosions, where the resistance of NiTi alloys is comparable to that of conventional alloys. It is attributed to the effect of work hardening [8]; nevertheless, the effect of NiTi alloys pseudoelastic behavior is mostly responsible for good wear resistance [9,10]. In addition, NiTi possesses damping-sensitive properties that make it a good candidate for material robots and smart materials actuators in the areas of micro-electro-mechanical system (MEMS) devices [11,12]. Although the hardness of NiTi

SMAs is much lower, better wear resistance has been reported as compared to those of conventional wear-resistant materials such as steel and alloy [13,14]. The effect of the sintering temperature on the microstructural evolution and transformation was studied in the case of SPS NiTi alloy [15,16]. Especially, NiTi alloys exhibit a higher wear resistance than conventional materials such as steels, and Co-based tribo-alloys and thus become a potential candidate for tribological applications [17,18]. The higher wear resistance of NiTi alloy is attributed to its so-called pseudoelasticity that is caused by reversible martensitic transformation. The sliding wear behaviors of NiTi alloy are derived from three different phases such as austenitic, martensitic, and dual-phase states of intermetallics. The austenitic phase has higher wear resistance than the martensitic phase of NiTi alloy [19]. On the other hand, it has been observed that the effect of nickel addition on the microstructure and wear behavior of spark-plasma-sintered CP-titanium, asserting an improved resistance to adhesive and abrasive wear with increasing nickel content [20]. However, there is an ambiguity in understanding the surface hardness contribution in terms of tribological behavior of NiTi alloys. In our previous work, we successfully prepared NiTi alloys with a shape memory effect [21]. Because of the tremendous application potential of NiTi, it is important to explore its durability from the tribological point of view. The understanding and control of the tribological behavior, as well as the overall mechanical durability of NiTi alloy prepared by the SPS technique, is an important issue. Interfacial phenomena such as adhesion, friction, and wear can affect the performance and durability of the devices made up of NiTi thick alloy.

In the present work, the tribological behaviors of NiTi alloy prepared by the SPS method and after various annealing have been studied using indentation, scratch, and wear tests. The aim is to understand the tribological response of NiTi alloy prepared by the alternative route and the effect of annealing on the wear response of the material. The wear mechanisms are analyzed in conjunction with phase formation during the annealing of NiTi alloy.

2. Materials and Methods

2.1. Materials

NiTi alloy samples were prepared by the SPS method using $Ti_{50}Ni_{50}$ powder (20–63 μm) at a temperature of 900 °C with a load of 48 MPa. The comprehensive characterization of the SPS NiTi alloy was described in our previous work [21]. The fabricated material was divided into four samples that were subsequently annealed (at different temperatures of 350, 450, and 550 °C in the air with a heating rate of 10 °C/min; cooling was spontaneous). One sample, labeled as NiTi_as-prepared, was kept as a reference. The samples were annealed in a conventional furnace for a 1 h duration. For the physical and tribo-mechanical testing, the samples were mirror-polished.

2.2. Experimental Methods

The surface features of the NiTi samples were analyzed by using a scanning electron microscope, Tescan FERA 3, dual-beam SEM/FIB equipped with a field emission cathode (Tescan Orsay Holding a.s., Brno, Czech Republic). The quality of the surface features was examined as a function of annealing temperature.

XRD data were collected at room temperature with an X'Pert PRO θ-θ powder diffractometer with a parafocusing Bragg-Brentano geometry at 40 mA and 35 kV with CoKα radiation (average wavelength λ = 0.1790 nm), a focus-slit distance of 100 mm, and a goniometer radius of 240 mm. The data were measured in the 2θ range of 20–120°, using a step size of 0.013°, a scan step time of 1.4 s, and a fixed divergence slit size of 0.5°. The phase analysis and the analysis of crystallite size and microstrain were performed using the software package HighScore Plus 4.8. fy. PANalytical. The NIST LaB_6 SRM 660a standard was used for the correction of the instrumental broadening.

Differential scanning calorimetry (DSC) analysis was carried out for the annealed samples by using a DSC 25 (TA Instruments, New Castle, DE, USA) instrument at a

scanning rate of 5 °C/min in the temperature range of −100 to +100 °C. The samples were cut into small pieces and placed inside an Al crucible that placed inside the chamber of a DSC furnace for measurement. Argon gas was used as purge gas during the experiments. The NiTi powder and the as-prepared NiTi alloy prepared by the SPS method showed the transformation temperature as a function of the cooling and heating temperatures is shown in previous work [21]. The transformation temperatures for the NiTi powder and the as-prepared NiTi alloy are included in the Table 1.

Table 1. Transformation temperatures for the annealed spark plasma sintering (SPS) samples.

Sample	A_s (°C)	A_f (°C)	R_s (°C)	R_f (°C)	M_s (°C)	M_f (°C)
NiTi_as-prepared	−47.6	29.7	-	-	−19	−47.6
NiTi powder	32	62	40	−2	−19	−47.6
NiTi_350 °C	32.39	52.34	44.98	13.47		-
NiTi_450 °C	17.34	38.48	39.27	21.61	−16.67	−53.99
NiTi_550 °C	−8.95	4.70	−14.14	−33.46	−35.03	−48.28

Mechanical and tribological properties were measured at room temperature by depth-sensing indentation (nanoindentation), and nano/microscratch and wear testing techniques using a fully calibrated NanoTest instrument (MicroMaterials Ltd., Wales, UK). The samples were fixed on a special low-noise/high-sensitivity acoustic emission (AE) sample holder employing a dedicated structured piezo-element and inbuilt pre-amplifier using a low-temperature wax.

Nanoindentation hardness and reduced elastic modulus were evaluated with a three-sided pyramidal Berkovich indenter at loads of 50 and 100 mN that corresponded to the maximum penetration depths around 750 and 1100 nm, respectively. Two loads were used to explore the possible effect of the lack of homogeneity and voids. The measured data were corrected for the thermal drift and the frame compliance of the instrument. Hardness and reduced elastic modulus values were calculated using a standard procedure [22]. The mean values and the standard deviation were calculated from at least 10 independent measurements.

Scratch tests and multi-pass wear tests were performed by a diamond Rockwell indenter with a nominal radius of 10 μm. During the progressive-load scratch test, the load on the indenter linearly increased after the first 50 μm until reaching the predefined maximum. The experiments were performed as a three-pass test, where the initial topography pass with a very low topography load of 0.02 mN was followed by the on-load scratch pass and later by the final topography pass to scan the scratch groove profile. Each test was repeated at least three times. Adhesion-cohesion properties were investigated with progressive-load load tests up to 100, 250, and 500 mN. The wear resistance was tested at the constant loads of 100 and 250 mN by a repetitive nanoscratch test with a total scan length of 450 μm and at a scanning speed of 10 μm/s. The gradual degradation of the surface layer was studied during 10 on-load passes; one topography pass was always alternated by two on-load passes. The scratch test and the wear test were evaluated based on a combined approach employing the analysis of the indenter load-depth records and the microscopic observation of residual wear tracks integrated with the AE records. The residual scratch grooves and wear tracks were thoroughly investigated with a laser scanning confocal microscope LEXT 5000 (Olympus, Tokyo, Japan) using depth and intensity (wavelength: 405 nm) images.

The AE activity was continuously monitored during the scratch and wear tests using the ZEDO system (Dakel, Prague, Czech Republic) featuring a high dynamic range and sampling frequencies as high as 10 MHz that enabled to explore very weak as well strong AE events at nano/microsecond scales in a broad frequency range of 30–2000 kHz. The direct correlation between the depth-load-distance/load records and AE records was ensured via the proper synchronization of the nanotester and the AE system.

3. Results and Discussion

The surface morphologies of the annealed NiTi samples are shown in Figure 1. There was no significant grain growth observed in the samples. The particles packing and necking was observed in each sample.
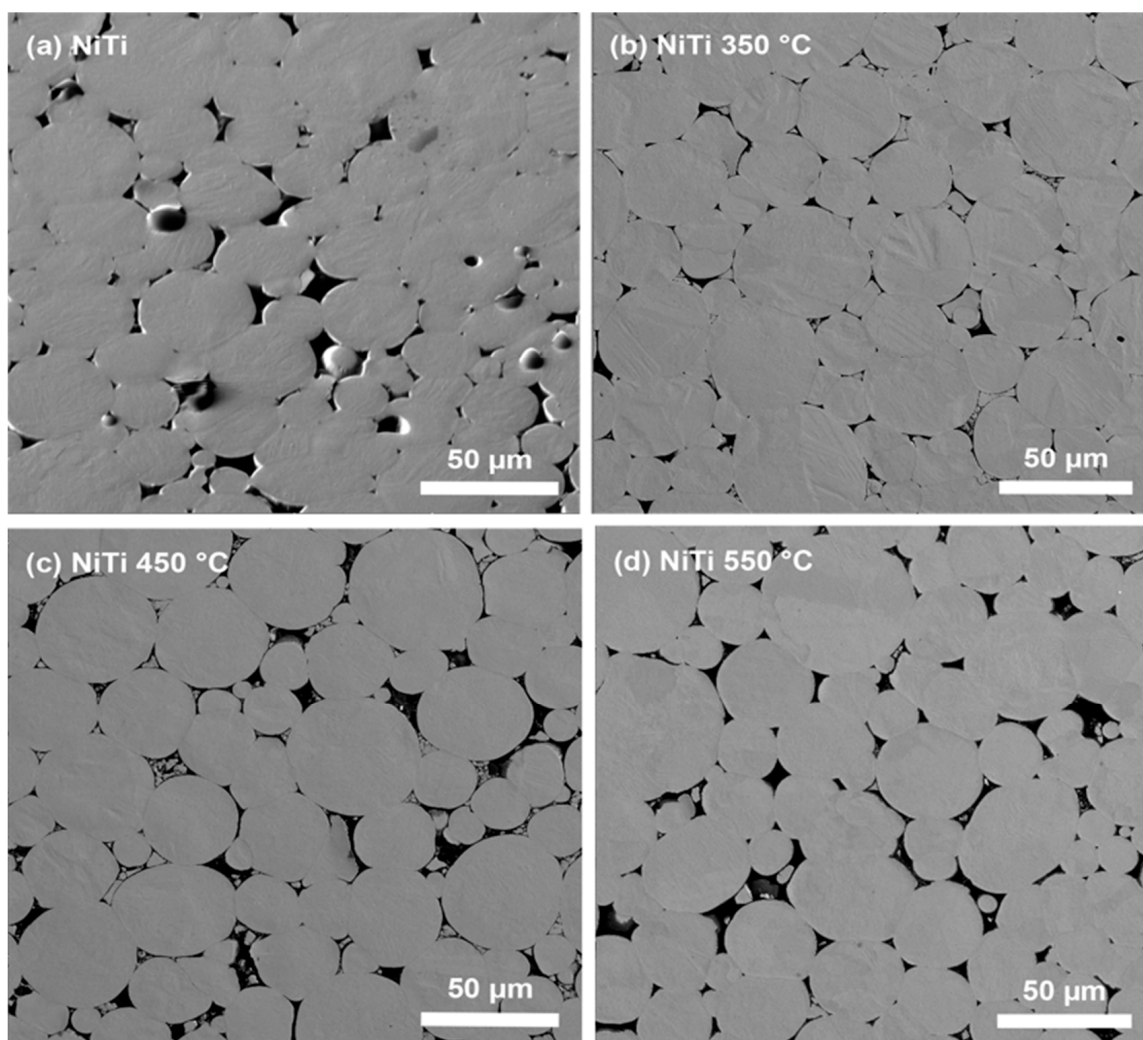
Figure 1. Backscattered SEM images of the (**a**) NiTi sample and annealed at (**b**) 350 °C, (**c**) 450 °C, and (**d**) 550 °C.

3.1. DSC Analysis of the NiTi Alloy and the Annealed NiTi Alloys

The phase transformation corresponding to the transformation temperature in the annealed NiTi samples was investigated by using DSC (Figure 2). The transformation temperature upon cooling changed from the austenite to the R-phase and finally towards martensitic transformation, indicating the martensite start and finish temperatures (M_s and M_f). Upon heating, the samples returned to the austenite phase with an indication of the start and finish temperatures (A_s and A_f). The shifting of the transformation temperature towards a lower temperature was observed. The transformation temperatures of the annealed samples are presented in Table 1.

The transformation peaks for the annealed samples showed the phases of the martensite, R-phase, and austenite start and finish temperatures. There were the prominent peaks of the austenite and R-phase observed in the annealed sample at 350 °C. At 450 °C, a bifurcating peak formed at the heating cycle that represented the combination of the R-phase with austenite. On cooling, the R-phase and martensite were separate. There was a shift towards a lower temperature upon more annealing at 550 °C. These peaks were very

prominent and distinguished in the sample after annealed. This shifting may happen due to the presence of intermetallic compounds.
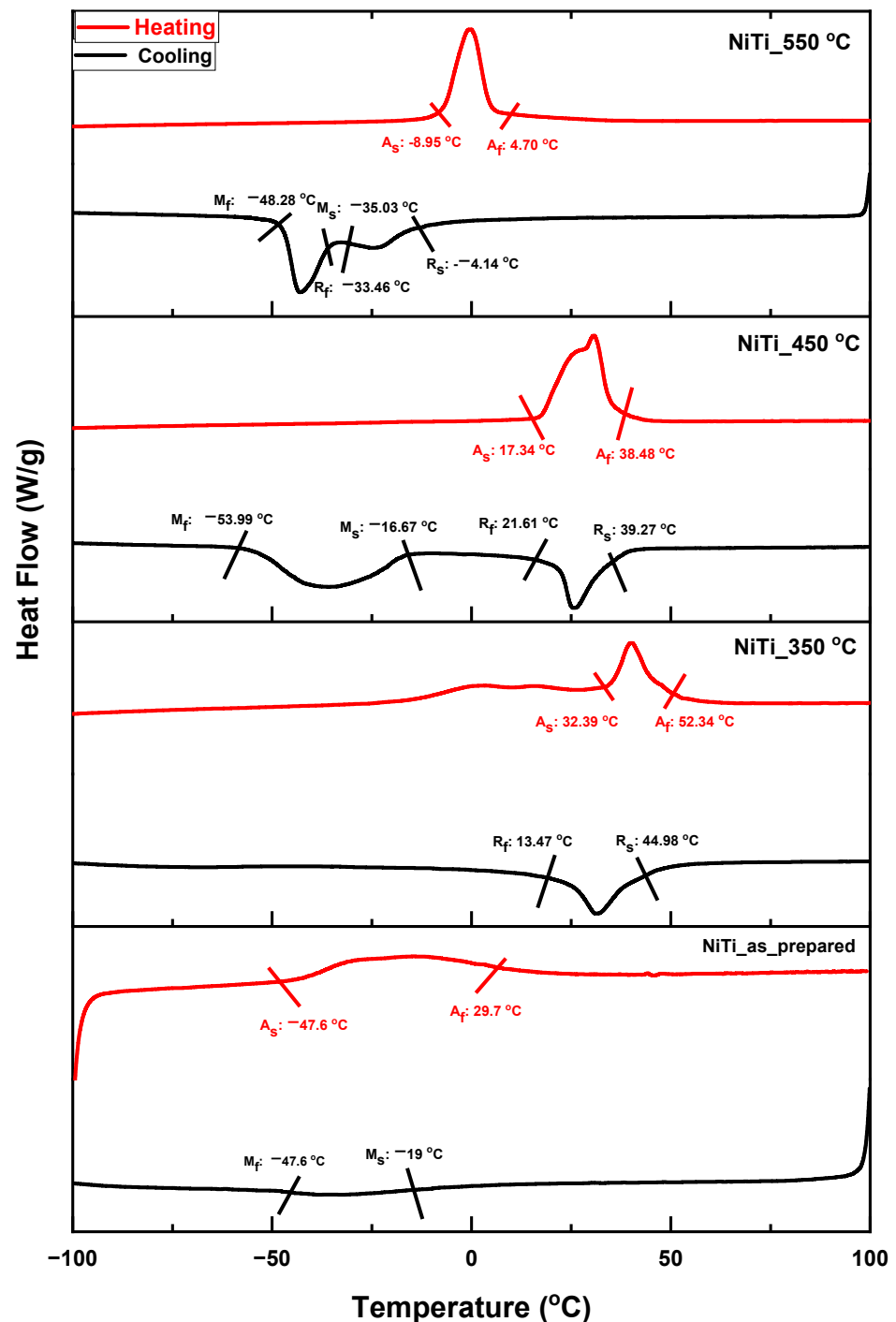
Figure 2. Differential scanning calorimetry (DSC) responses of the annealed SPS NiTi samples showing the heat flow as a function of temperature.

3.2. XRD Analysis of the NiTi Alloy and the Annealed NiTi Alloys

The phase composition, particle size, and strain of the NiTi powder, the as-prepared NiTi alloy (NiTi_as-prepared), and its corresponding annealed samples were evaluated via XRD. The diffractograms of the starting powder NiTi and the as-prepared NiTi alloy are shown in Figure 3a.
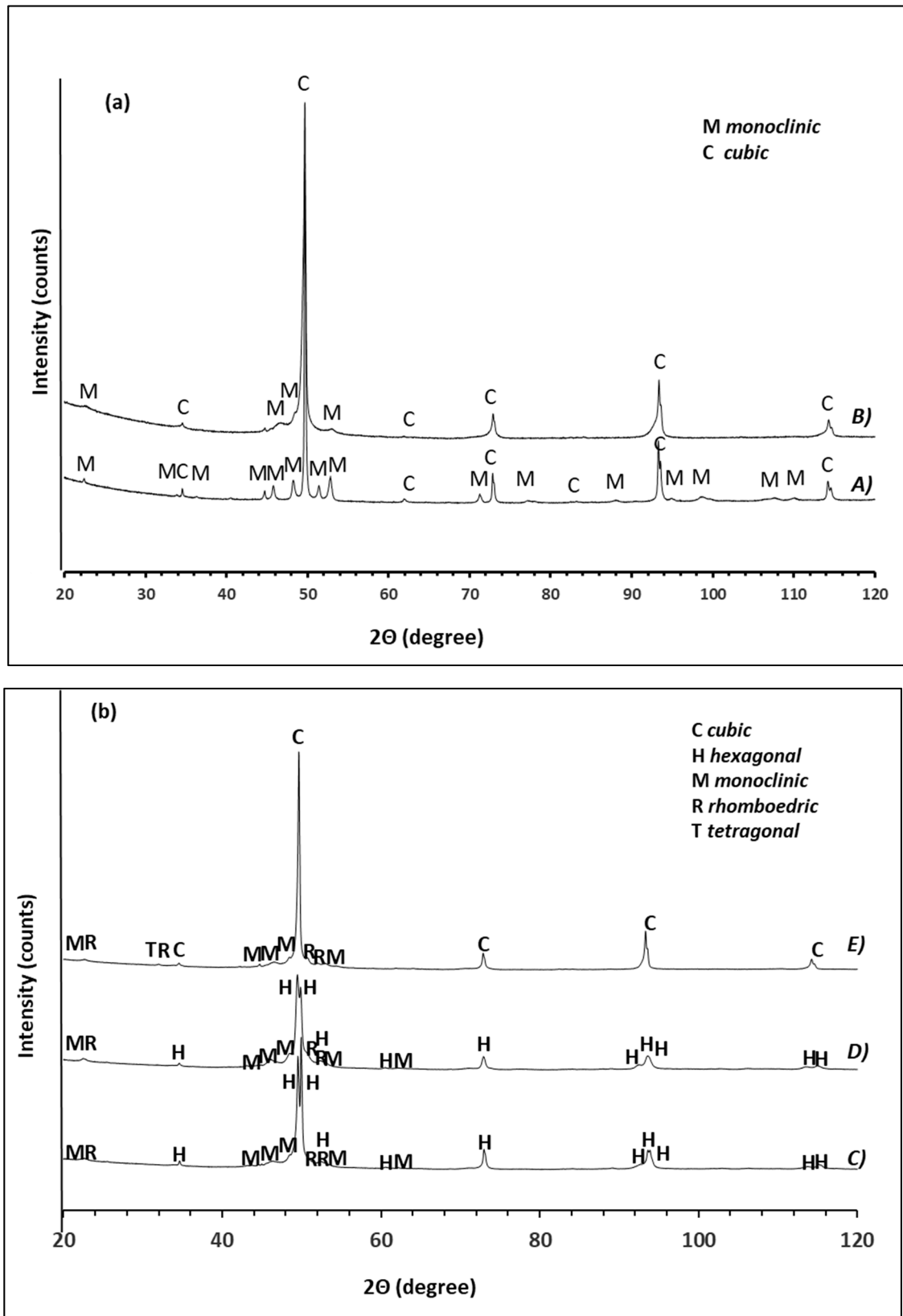
Figure 3. (**a**). Powder XRD patterns of *A*) NiTi particles and *B*) NiTi as_prepared. (**b**) Powder XRD patterns of the NiTi alloys annealed at *C*) 350 °C, *D*) 450 °C, and *E*) 550 °C.

Since both systems turned out to be two-phase and after compaction a significantly different broadening of the peaks appeared, multicomponent and multiline Rietveld re-

finement was used to calculate the quantitative phase composition. From independent and well separable diffraction peaks, it was possible to construct a Langford plot for the calculation of coherent particle size and microstrain. The same calculation method could be used for the annealed samples. The quantitative estimation of various phases, as well as the results of size/strain analysis for the NiTi powder and the annealed samples, are summarized in Table 2.

Table 2. Phase compositions, crystallite sizes, and strains of the NiTi powder, the as-prepared NiTi by SPS, and the annealed samples.

Sample	Phase/Lattice	Space Group	Content (% m/m)	R_{Bragg}	Crystallite Size (nm)	Strain (%)	$R_{profile}$	D-stat
NiTi particles	NiTi cubic	Pm-3m	78.5	6.22	74.8	0.03	0.63	1.72
	NiTi monoclinic	P2$_1$/m	21.5	7.84	25.2	0.10	1.88	0.73
NiTi_as-prepared	NiTi cubic	Pm-3m	77.7	1.43	30.2	0.00	1.69	0.21
	NiTi monoclinic	P2$_1$/m	22.3	1.22	6.3	1.00	1.69	0.21
	NiTi trigonal	P-3	71.7	2.48	33.1	0.10	1.27	0.43
NiTi_350 °C	NiTi monoclinic	P2$_1$/m	16.2	3.49	7.7	1.00	1.37	0.31
	Ni$_4$Ti$_3$ rhomboedric	R-3	12.1	3.97	NC	NC	NC	NC
	NiTi trigonal	P-3	61.8	0.12	28	0.20	1.11	0.63
NiTi_450 °C	NiTi monoclinic	P2$_1$/m	25.5	0.28	15.5	1.00	1.08	0.70
	Ni$_4$Ti$_3$ rhomboedric	R-3	12.7	0.27	NC	NC	NC	NC
	NiTi cubic	Pm-3m	88.5	3.88	25	0.00	1.90	0.12
NiTi_550 °C	NiTi monoclinic	P2$_1$/m	4.4	1.19	7.5	0.00	1.88	0.12
	Ni$_4$Ti$_3$ rhomboedric	R-3	6.5	2.22	NC	NC	NC	NC
	TiO$_2$ tetragonal	P42/mmm	0.6	0.98	NC	NC	NC	NC

Both the starting powder and the SPS as-prepared alloy showed the same qualitative and very similar quantitative phase compositions; 78.5 resp. 77.7 wt.% of austenite and 21.5 resp. 22.3 wt.% of the martensite phase. The crystallite size of the austenite phase decreased by the SPS method from 74.8 to 30.2 nm. On the annealed sample at 550 °C, the crystallite size for austenite further decreased to 25 nm. The crystallite size of the monoclinic phase was reduced to 7.5 nm. The samples annealed at the temperatures of 350 and 450 °C showed metastable behaviors with the presence of R-phase. The minimum strain of 0.1% was observed in the NiTi_as-prepared sample. The minimum strain was maintained or increased in the samples annealed at 350 and 450 °C. However, the sample annealed at 550 °C did not show any strain. The crystallite size of the martensite phase decreased from 25.2 to 7.7 nm with a minimized strain.

In the case of the annealed samples, the evolutions of the phase composition and the coherent particle size as a function of the sintering temperature were observed (see Figure 3b). Upon annealing, the NiTi alloys at various heating temperatures of 350, 450, and 550 °C for 1 h in the presence of some intermetallic compounds were identified. The sample annealed at 350 °C showed the presence of the R-phase (trigonal, 71.7%), the martensite phase (monoclinic, 16.2%), and the intermetallic compound Ni$_3$Ti$_4$ (rhomboedric phase, 12.1%). At 450 °C, the sample showed a hexagonal phase of 61.8% and a monoclinic phase of martensite 25.5% with an intermetallic phase of 12.7%. The sample annealed at 550 °C showed 88.5% of the austenite phase with 4.4 wt % of the martensite phase, intermetallic compound Ni$_3$Ti$_4$ of 6.6 wt % with some minor quantity of the rutile phase. The premartensitic phase (so-called R-phase) with a trigonal P-3 structure emerged in the annealed samples may arise due to the thermal effect in the NiTi structure, leading to an asymmetric form. The R-phase was precisely trigonal; nevertheless, its trigonality was very weak, and in the literature, is sometimes marked as hexagonal, which is the same as in Figure 3b [23]. The intermetallic phases that may arise from the eutectoid decomposition of NiTi to NiTi$_2$, Ni$_3$Ti, or Ni$_3$Ti$_4$ formed results, when the preannealed samples were in the furnace [24]. The quantity of the intermetallic phase of Ni$_4$Ti$_3$ was approximately 12% in the annealed samples, which well agrees with other research results [21,22]. The increasing area fraction of the intermetallic compound and the oxide compound belonged to the undesirable side effects of the increasing heating temperature. While the crystallite size of the NiTi phase after SPS was 6.3 nm for the monoclinic martensitic phase, it increased after annealed at 350 °C and then significantly improved until the temperature reached 450 °C,

from 7.7 to 15.5 nm. However, the trend was not maintained as a function of the annealing temperature, this may attribute to the grain growth, but the grains contained the same amount of imperfections. Thus, the crystallite size did not change at the temperature of 550 °C, which did not follow the trend [25]. It was observed that the samples annealed at 350 and 450 °C showed a premartensitic phase (R-phase) with a trigonal structure, whereas the sample annealed at 550 °C showed only a cubic austenite phase. The decrease in particle size, together with the growth in microstrains, illustrated that the hexagonal lattice became unstable at increasing heating temperature and then underwent the final phase transformation into a cubic lattice system. Figure 3b displays the formation of intermetallic phases emerging in the annealed samples with a major conversion into the austenite phase at the maximum annealing temperature of 550 °C.

3.3. Nanoindentation of the NiTi Alloy and the Annealed NiTi Alloys

Sets of indentation curves, the calculated hardness, reduced modulus, and plasticity index values (ratio of the plastic to total indentation work) as a function of the annealing temperature are represented in Figure 4a–d. The hardness of the original (as-prepared) SPS sample showed a mean value of 4 GPa for both loads of 50 and 100 mN. After the annealing at 350 °C, the indentation hardness increased to approximately 4.5 GPa. On the other hand, a further increase of the annealing temperature led to a reduction of hardness even below that of the original SPS sample. This effect can be linked to the temperature-driven phase changes, more specifically to the transformation from the austenite phase to the R-phase. The elastic modulus values followed the same trend, while the maximum value of about 95 GPa was observed for the sample annealed at 350 °C. The indentation depth was inversely proportional to the hardness of the annealed SPS alloys.
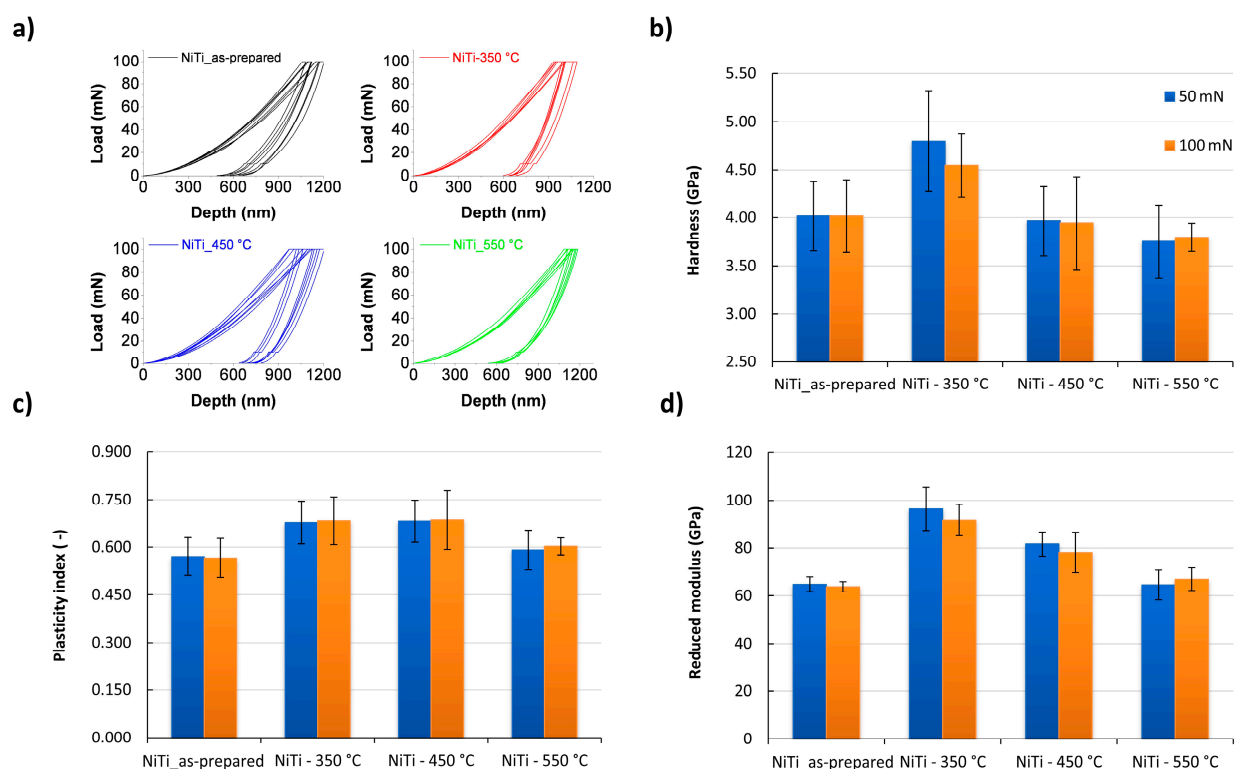
Figure 4. Results of nanoindentation tests on the as-prepared and annealed SPS samples of NiTi: (**a**) hardness; (**b**) reduced elastic modulus; (**c**) indentation curves for experiments up to 100 mN; (**d**) plasticity index.

It should be noted that hardness alone does not always provide enough information necessary for the prediction of wear. Therefore, new parameters, often ratios of easily

accessible basic parameters, have been introduced for the description of overall mechanical durability such as plasticity index, H/E ratio, and H^3/E^2 ratio) [26,27]. The plasticity index, defined as the ratio of plastic to total indentation work W_p/W_t that describes the amount of mechanical work spent for plastic deformation, initially increased with the annealing temperature, reached its maximum for 350 and 450 °C and then declined at 550 °C. This can be seen from a larger area enclosed by the indentation curve. Higher values of plasticity index reflected higher susceptibility to the plastic deformation of the samples annealed at 350 and 450 °C in comparison to the as-prepared sample and the annealed samples at 550 °C. An inverse behavior was observed for H/E and H^3/E^2 ratios with the lowest value of the H/E ratio or the highest E/H ratio for the annealed sample at 350 °C (see Figure 5). It should be noted that especially the plasticity index, the H/E ratio, and the H^3/E^2 ratio are often used as important parameters governing the overall mechanical durability [28,29]. Where the former is usually linked to the elastic strain to failure, while the later is defined as the resistance to plastic deformation. Furthermore, the H/E ratio predetermines the fracture behavior, as it appears in the majority of fracture toughness equations. The surface resistance to fracture initiation and propagation scales inversely with the H/E ratio [30,31].

a)   **b)**
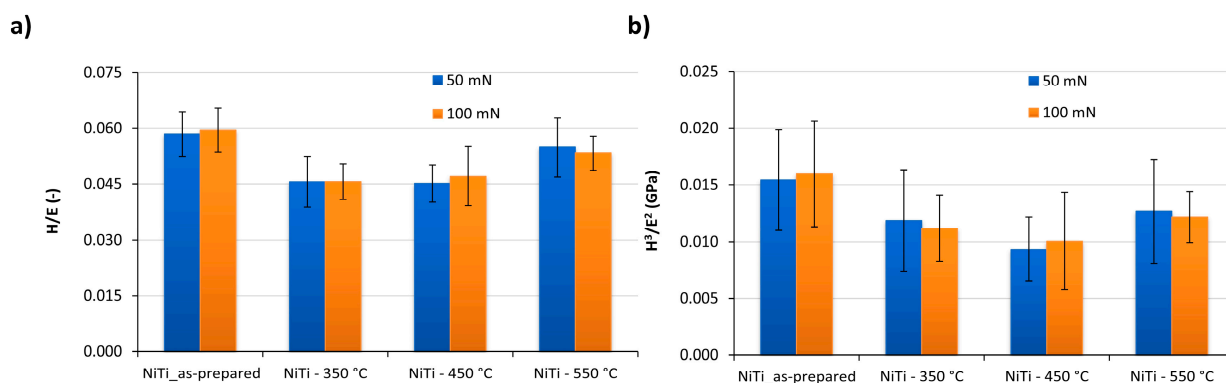
Figure 5. Hardness-to-elastic modulus ratios for the as-prepared and annealed SPS samples: (**a**) H/E ratio; (**b**) H^3/E^2 ratio.

3.4. Scratch and Wear Tests for the NiTi Alloy and the Annealed NiTi Alloys

The overview of the residual grooves after progressive-load scratch tests made with a spherical indenter is shown in Figure 6. The depth representation for tests performed at 500 mN pointed out the plastic deformation, as the dominant phenomenon was observed. The same held for a lower load of 250 mN, where a less extent of plastic deformation was distinguished as also evidenced by lower indentation depths in Figure 7. The detailed microscopic analysis (in both depth and intensity representations) did not reveal any traces of the cracking inside or the detachment between individual spherical particles forming the compact sample.

The depth change records in Figure 7 compared the on-load depths (blue curves) to the plastic depths of residual grooves (red curves) obtained using a final topographic scan. The 250 mN scratch test showed fewer fluctuations of on-load depth profiles for NiTi in the case annealed samples at 350 and 550 °C in comparison to those of the as-prepared sample and the sample annealed at 450 °C. The different degrees of porosity, together with the change in phase compositions, can be responsible for this behavior. In order to show a high repeatability for the explored spark-plasma-sintered samples, three profiles for each scratch test are presented in Figure 7.

The difference between the on-load (i.e., elastic-plastic) and residual (i.e., plastic) profiles in the graphs can be quantified via the elastic recovery parameter (ERP). The ERP value was obtained from the last 15 μm of the scratch length, where the maximum load was already held constant. Figure 8 shows the ERP values for the tested NiTi samples obtained from the 500 mN ramped-load scratches, where the surface deformation was well developed. Curves with a non-standard shape of the final part of the scratch, usually

caused by a pore (void) between the individual particles, were excluded. The lowest values of the ERP were measured for the as-prepared sample and the annealed NiTi sample at 550 °C containing the austenitic phase, while the ERP value increased by an average of 15% for the samples annealed at 350 and 450 °C.

Based on the results of the ramped-load scratch tests, the constant load multi-pass wear tests were performed on given samples at two loads, 100 and 250 mN. Their evaluation was conducted from depth records, primarily through monitoring depth increments between on-load or topographic passes. Furthermore, the wear rate was calculated as the worn volume per unit distance using the depth records and the three-dimensional (3D) microscopic data of the residual wear tracks. The typical residual wear tracks are shown in Figure 9 for tests performed at 250 mN with more pronounced plastic deformation.
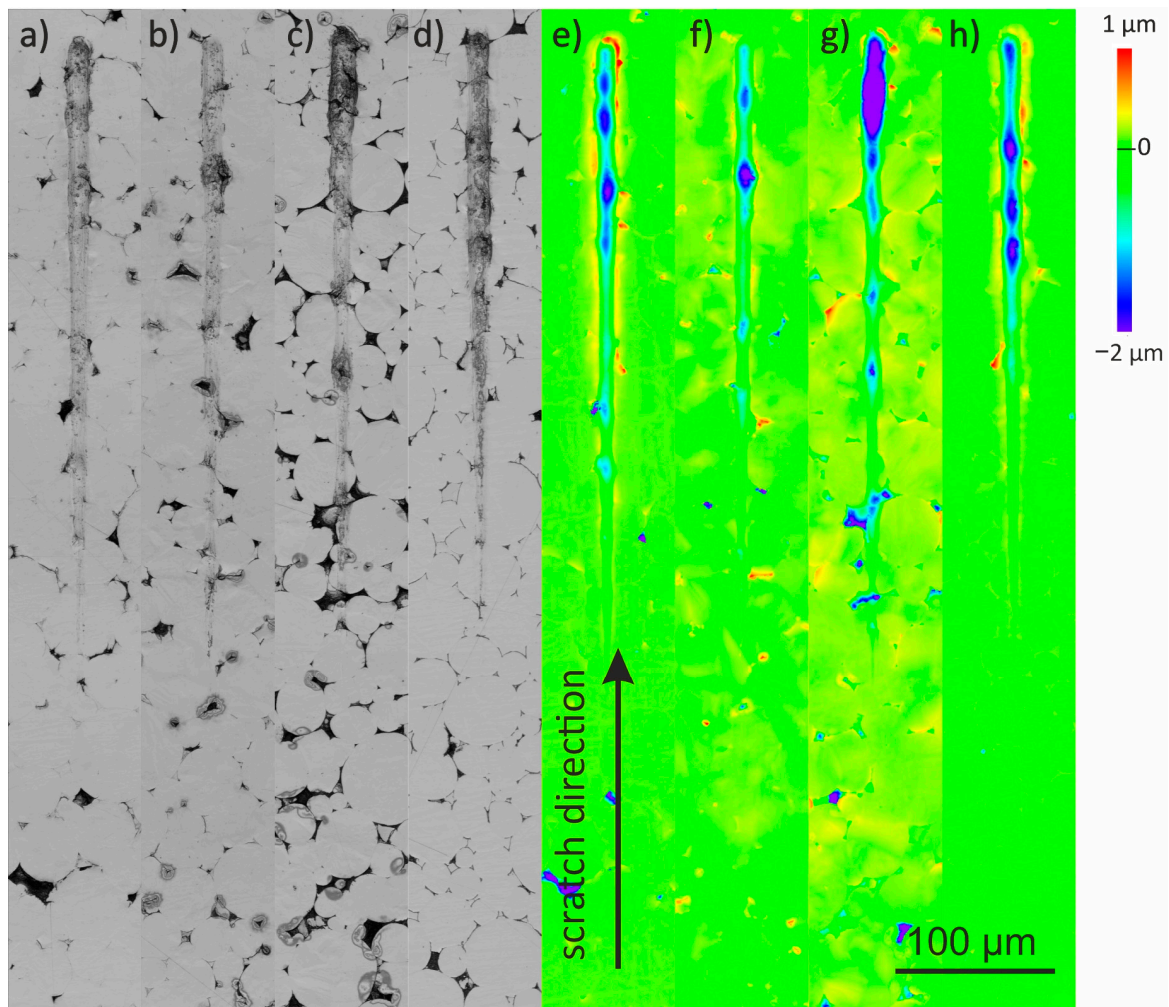
Figure 6. Typical residual scratch grooves after progressive-load scratch tests on the NiTi samples (as-prepared and annealed) made at a normal load of 500 mN in intensity and depth representations for the as-prepared sample (**a**,**e**) and the samples annealed at 350 °C (**b**,**f**), 450 °C (**c**,**g**), and 550 °C (**d**,**h**).
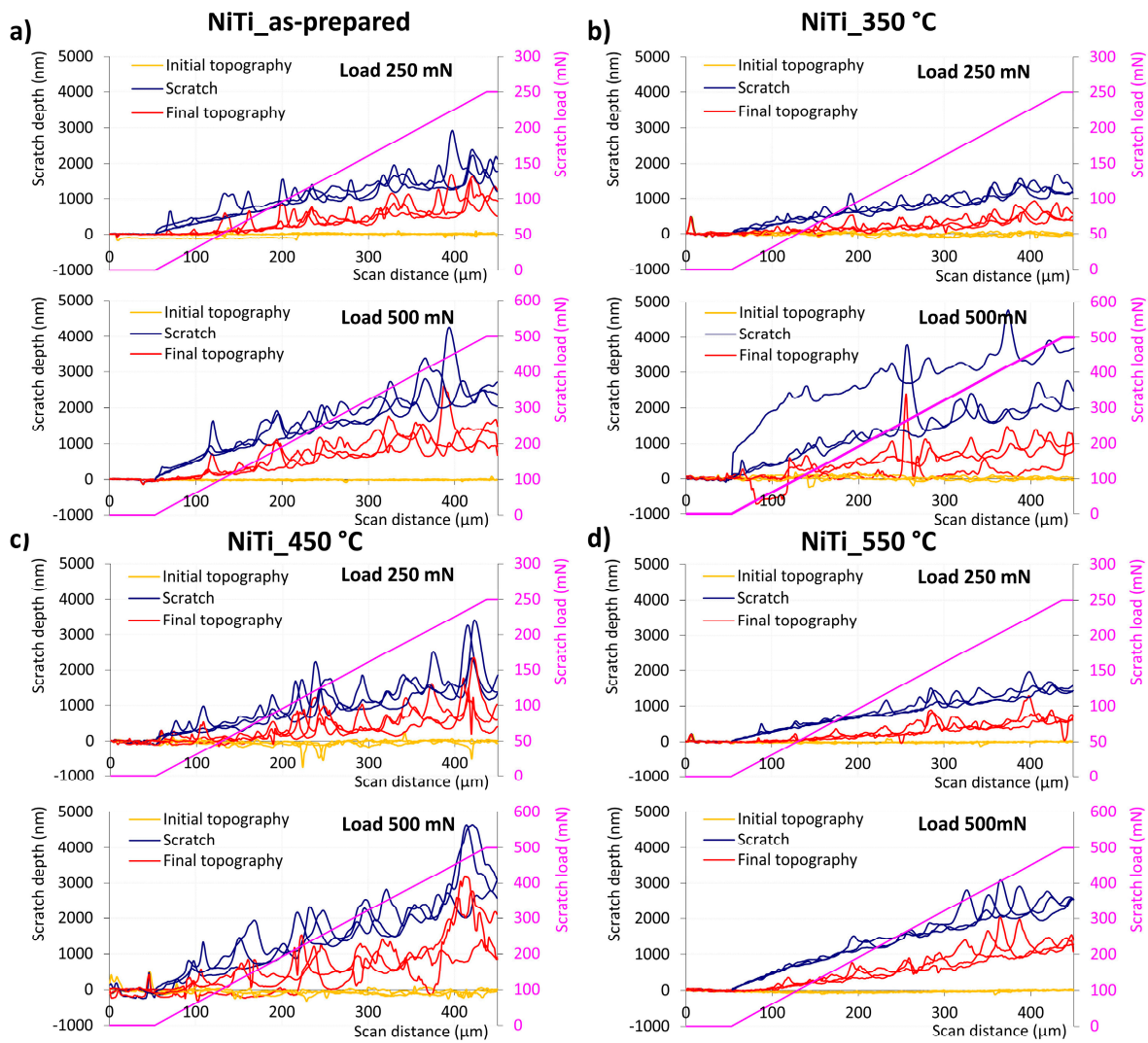
Figure 7. Depth change records of 250 and 500 mN progressive-load scratch tests of the as-prepared NiTi sample (**a**), NiTi annealed at 350 °C (**b**), NiTi annealed at 450 °C (**c**), and NiTi annealed at 550 °C (**d**) (depth profiles for 3 independent tests are presented in each graph).
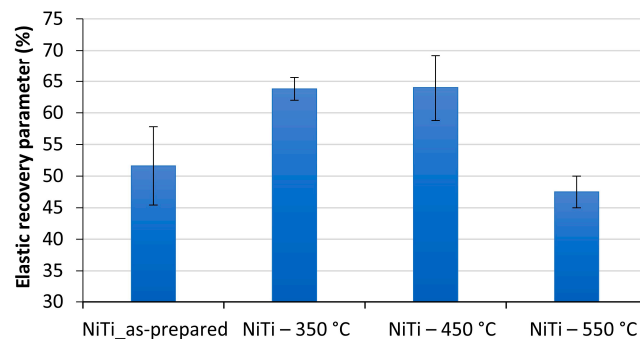
Figure 8. Elastic recovery parameters obtained from the last part of the 500 mN ramped-load scratch test for NiTi_as-prepared, NiTi annealed at 350 °C, NiTi annealed at 450 °C, and NiTi annealed at 550 °C.
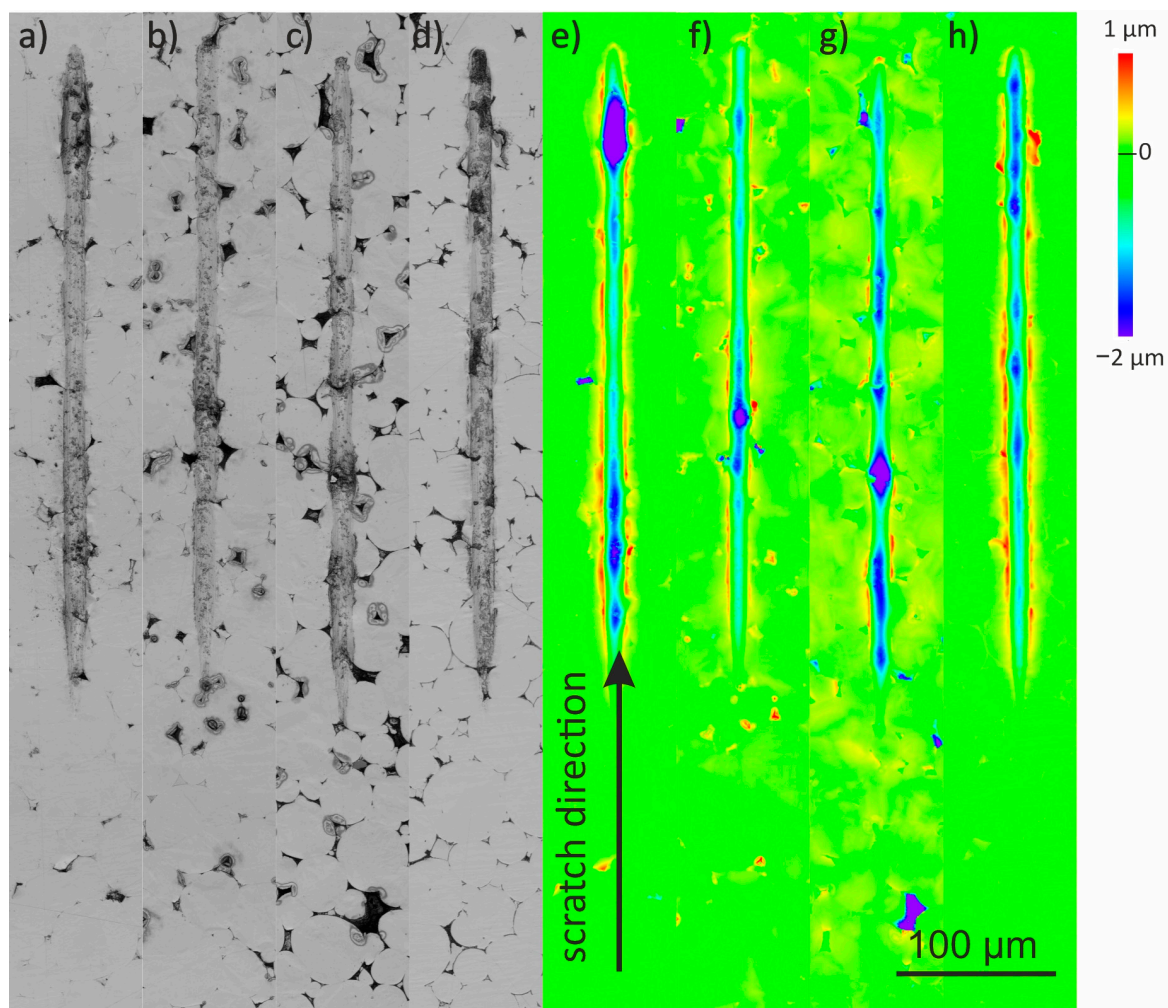
Figure 9. Typical residual wear tracks after constant-load multi-pass wear on NiTi samples (as-prepared and annealed) made at a normal load of 250 mN in intensity and depth representation for the as-prepared sample (**a**,**e**) and the samples annealed at 350 °C (**b**,**f**), 450 °C (**c**,**g**), and 550 °C (**d**,**h**).

The depth increments analysis of the multi-pass wear test did not reveal significant differences between the investigated NiTi samples. Only the as-prepared NiTi sample (NiTi_as-prepared) reached slightly higher on-load depths than the NiTi sample annealed at 350 °C, which correlated well with the higher hardness for the latter sample determined using nanoindentation. The resulting records from the wear tests were relatively smooth, with the curve fluctuating only in the case of the NiTi sample annealed at 450 °C, which may correspond to the surface/near subsurface inhomogeneity or the decrease of particle compactness. Similar trends were observed also for the test performed at 100 mN.

The comparison of wear rates calculated based on the evaluation of the residual wear tracks using 3D microscopy and depth records is shown in Figure 10b. Although the absolute values differed, trends remained quantitatively similar. In general, the discrepancy between these two independent approaches originates from both the porosity of samples and the methods peculiarities. The worn volume was directly evaluated via 3D microscopy, while the geometric relations were applied to the depth records. The higher spatial resolution of the optical method was then responsible for the incorporation of the pores volume inside the residual wear track, resulting in the increased value of the worn volume. On the other hand, the profilometry was performed using the same diamond tip (radius: 10 μm) like the on-load passes and was less sensitive to pores contribution.
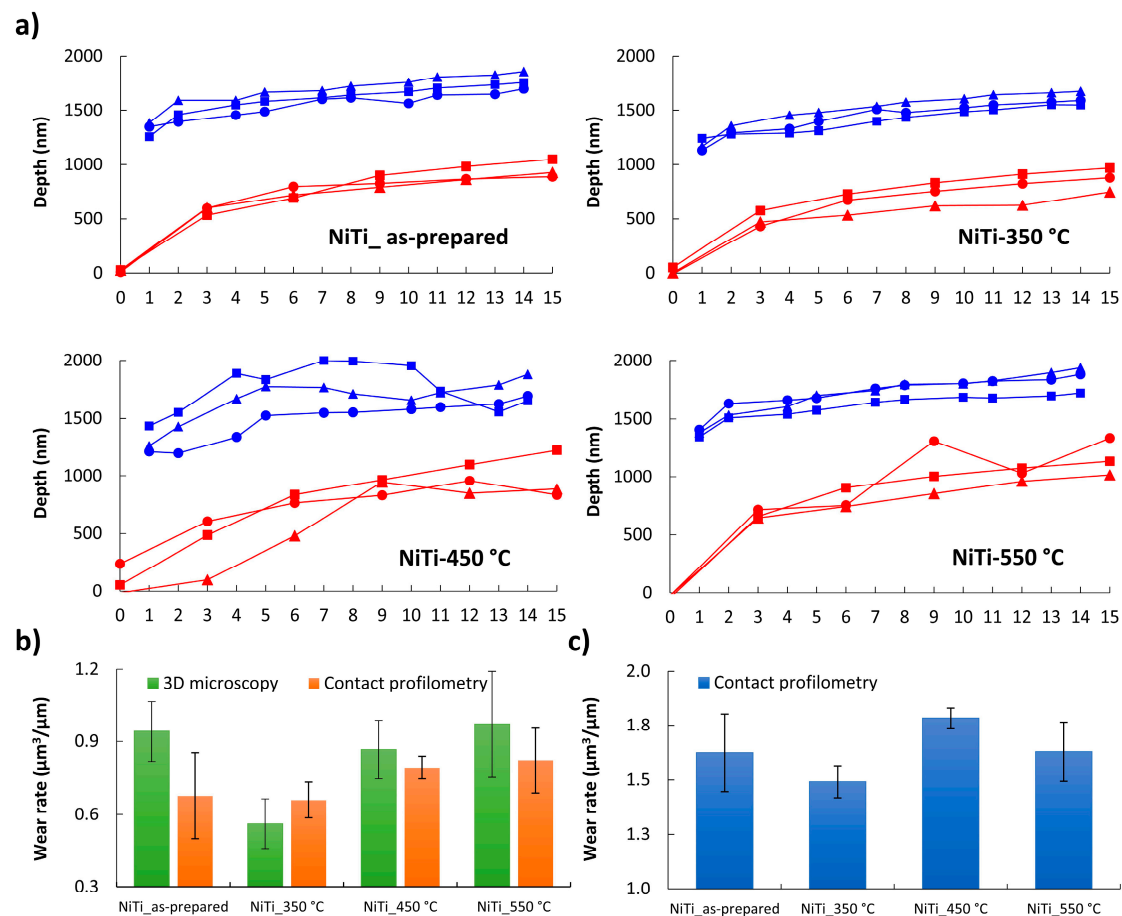
Figure 10. Evaluation of the constant-load multi-pass wear tests performed at 250 mN: (**a**) on-load (blue) and the topography (red) depth increments records; (**b**) wear rates calculated from residual wear tracks (topographic data); (**c**) wear rates calculated from the on-load data.

The lowest wear rate was observed for the sample annealed at 350 °C, while the highest wear rate was found for the as-prepared sample and the annealed sample at 550 °C. This behavior correlated with the hardness values (Figure 4b) and the classical Archards wear theory [32] that directly relates the hardness to the worn volume. The increased worn volume for NiTi_as-prepared and NiTi_550 °C can be linked to a larger amount of the plastically displaced material as evidenced in Figure 9e,h and also to a lower amount of the ERP (see Figure 8). It should be noted that this analysis considers only the shape and dimension of the residual wear track, in other words, it reflects only the permanent plastic deformation. Taking into the account the on-load depth record for the final pass, it is possible to calculate the worn volume and the wear rate for the combined conditions of elastic and plastic deformation (see Figure 10c). Similarly to the previous case, the smallest wear rate was observed in the hardest NiTi_350 °C sample.

The AE envelopes, representing the signal detected during the scratch test and coming from the sudden microstructural rearrangement of the SPS samples, are shown in Figure 11. A pronounced AE activity was detected for the as-prepared sample, while the annealed samples either exhibited only a very faint AE activity or did not exhibit it at all. Therefore, only the AE activities of the as-prepared sample and the sample annealed at 350 °C were presented. It can be seen that the detection threshold for the as-prepared sample, i.e., the occurrence of the first AE activity, shifted to the earlier stages of the test with the increase of the normal load [33]. In order to better understand the nature and origin of the AE signal, one can see a composite graph in Figure 12 showing the AE envelope and the corresponding depth change record together with the residual scratch groove. The AE signal was clearly distinguishable, and the highest AE amplitudes mostly accompanied

sudden changes in the penetration depth. Nevertheless, there were many other clearly visible AE events. This implied that the interfacial cracking between individual particles (particles detachment) was not the single failure mechanism [34,35]. On the contrary, the absence of the detectable AE signal suggested the improvement of the particles boundaries as well as the modified crystallinity for the annealed samples.
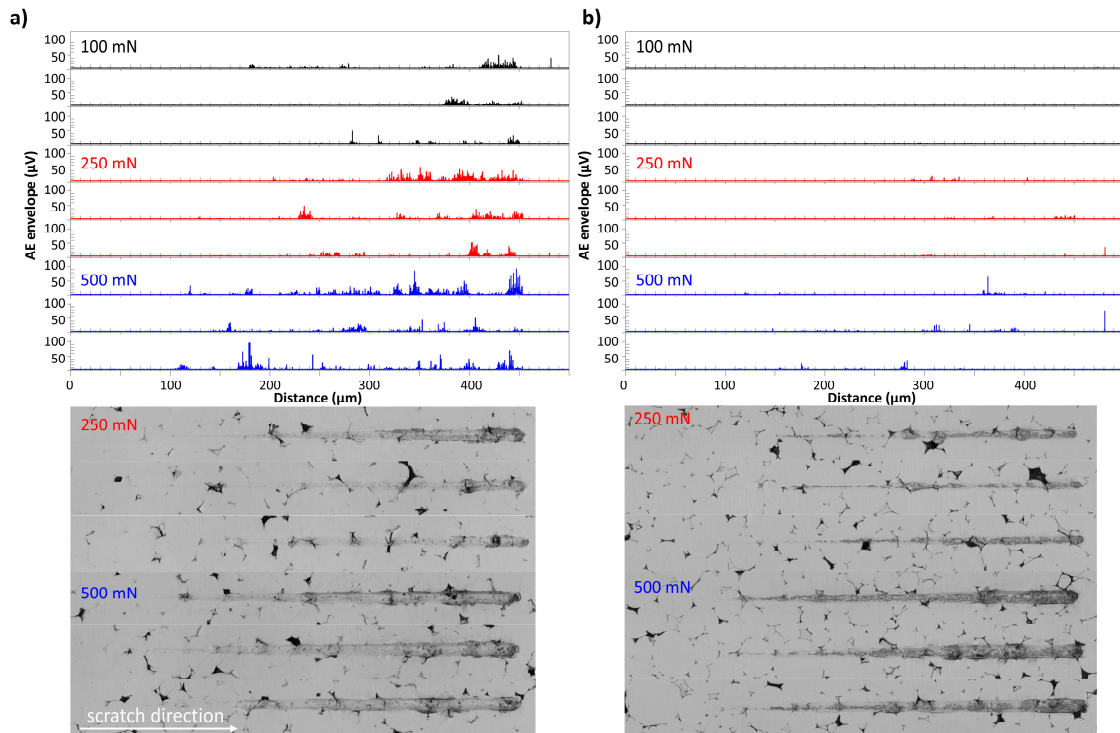
Figure 11. Acoustic emission (AE) envelopes recorded during progressive-load scratch tests performed up to 100, 250, and 500 mN for the as-prepared sample (**a**) and the air-annealed sample at 350 °C (**b**) (3 records for each normal load are presented to show repeatability).
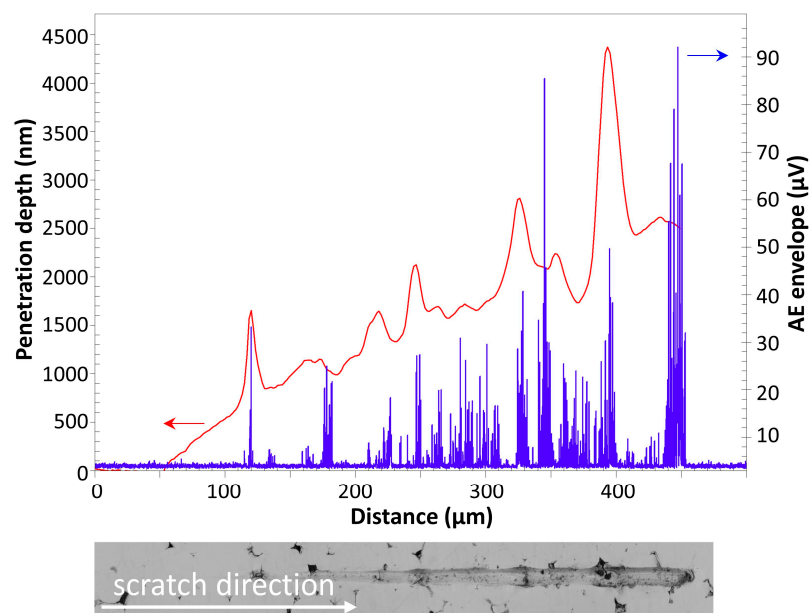
Figure 12. Typical depth change record together with the corresponding AE envelope for the progressive-load scratch test performed up to 500 mN on the sample NiTi_as-prepared.

The formation of the native oxide scale after annealing at 550 °C was identified by XRD as the titania rutile phase. The presence of this oxide scale acting as the tribolayer can be responsible for the improved cracking resistance of the annealed SPS samples [36–38]. It should be noted that the rhomboedric phase was observed for the annealed samples and the austenite phase becames dominant after annealing at 550 °C (see Table 2).

Although the depth change records and the microscopic observation identified only faint differences in durability, the analysis of AE records obtained during the multi-pass wear tests revealed different behaviors of the SPS samples. The as-prepared sample exhibited a distinct AE activity during the first three load passes, while the amplitude of AE events vanished gradually in the course of the test. On the other hand, weak AE activities were detected for the annealed samples only during the first two load passes (see Figure 13. Besides, an AE activity was observed at specific places repeatably that reflected the presence of surface voids. The particle boundary delamination or crushing for the as-prepared samples supported the hypothesis of improved mechanical durability in the case of the annealed samples. This clearly evidences that AE is a valuable method providing a unique insight into the deformation response of materials at an external loading [22,32,33,39,40].
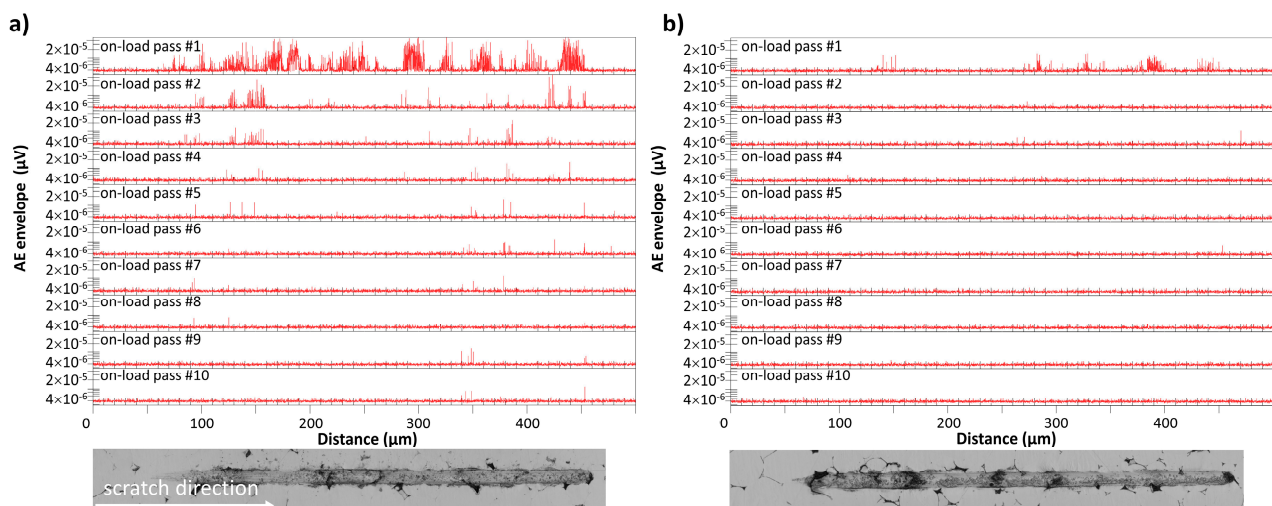
Figure 13. AE envelopes for the multi-pass wear tests performed at 250 mN for the NiTi_as-prepared samples (**a**) and the annealed sample at 350 °C (**b**).

The wear behavior was influenced by the presence of the precipitates of intermetallic phases such as Ni_3Ti_4 with a high capacity of transformations into the austenite phase. This resulted in an increased absorbed energy for the transformation of the structure that led to a decrease in the damage mechanism. The annealed samples contained more martensite phases, which could be easily oriented, reoriented and re-transformed within the structures during the wear test without any absorption of energy. This led to no significant change in the wear test. The presence of precipitate phases strongly affected the hardness and the wear behavior, as the nucleation, free-growth, mobility, and accommodation of phases were restricted which conditioned the capacity for absorbing energy reducing the wear damage [41–44].

The plethora of results obtained via all the performed local mechanical tests and structural investigation clearly manifested a complex nature of the mechanical and tribological durability of the spark-plasma-sintered NiTi samples. The phase composition was significantly affected by the annealing temperature that in turn directly changed mechanical properties and surface durability. The highest hardness and elastic modulus values for the sample annealed at 350 °C well agreed with lower penetration scratch depths as well as the smallest volume of material pile-uped around the edges of residual scratch grooves.

This was also supported by higher values of the scratch ERP in comparison to austenite containing the NiTi_as-prepared and NiTi_550 °C samples. The opposite trends between indentation plasticity index and scratch elastic recovery parameter can be explained by a different nature of loading conditions including the strain rate and the friction. This complexity of specific loading conditions and crystallographic phase mixture also contradicted the commonly used assumption that H/E scales with wear resistance. It was also reported that the resistance to plastic deformation, defined as the H3/E2 ratio, does not always directly increases with the threshold for nonelastic deformation as reported for dynamic contact [40]. This suggests that classical Archard theory relating the hardness to the wear rate holds for NiTi, at least under the loading conditions used in this study. The wear rate calculated for the conditions of purely plastic deformation (analysis of the residual wear track—final depth) as well as the combined elastic and plastic deformation (on load depth) implied the best performance of the sample annealed at 350 °C with a specific mixture of crystallographic phases. The specific phase composition was then probably responsible for a more effective energy dissipation mechanism and better tribomechanical durability. Although the titania tribolayer was identified for the annealed sample at 550 °C, its effect on the improvement of the overall tribological performance was not observed. In general, a positive effect of annealing on the improved fracture resistivity was identified via AE monitoring during the local tribo/mechanical testing.

4. Conclusions

The tribological and structural investigations of NiTi alloy samples prepared by the SPS method were performed before and after annealing. The SPS method proved to be an alternative route for the preparation of NiTi SMA. Depth sensing indentation, scratch testing, and wear testing coupled with AE detection were performed at various loading conditions. After annealing at 350 °C, NiTi alloy showed a phase change from the austenite to the R-phase with some martensite and intermetallic compounds. Further investigations need to be conducted to determine the surface recovery of indentation points based on the shape memory effect of NiTi alloys. The influence of annealing on the formation of additional phases and its role in surface recovery are also worth further study. For the NiTi alloy annealed at 350 °C, the wear behavior was also influenced by the presence of precipitate intermetallic phases of Ni_4Ti_3 as well as its high capacity of transformation, which increased the absorbed energy for restoring the structure and then decreasing the damage mechanism.

Institutional Review Board Statement: Not applicable.

Informed Consent Statement: Not applicable.

Data Availability Statement: Data will be available upon request from researchers.

Conflicts of Interest: The authors declare no conflict of interest.

References

1. Otsuka, K.; Ren, X. Physical metallurgy of Ti-Ni based shape memory alloys. *Prog. Mater. Sci.* **2005**, *50*, 511–678. [CrossRef]
2. Van Humbeeck, J. Shape Memory Alloys: A Material and a Technology. *Adv. Eng. Mater.* **2001**, *3*, 837–850. [CrossRef]
3. Wang, F.E.; Buehler, W.J.; Pickart, S.J. Crystal structure and a unique "martensitic" transition of TiNi. *J. Appl. Phys.* **1965**, *36*, 3232. [CrossRef]
4. Ball, A. On the importance of work hardening in the design of wear-resistant materials. *Wear* **1983**, *91*, 201. [CrossRef]
5. El Feninat, F.; Laroche, G.; Fiset, M.; Mantovani, D. Shape memory materials for biomedical applications. *Adv. Eng. Mater.* **2002**, *4*, 91–104. [CrossRef]
6. Geetha, M.; Singh, A.K.; Asokamani, R.; Gogia, A.K. Ti based biomaterials, the ultimate choice for orthopedic implants—A review. *Prog. Mater. Sci.* **2009**, *54*, 397–425. [CrossRef]
7. Liang, Y.N.; Li, S.Z.; Jin, Y.B.; Jin, W.; Li, S. Wear behavior of a TiNi alloy. *Wear* **1996**, *198*, 236–241. [CrossRef]
8. Shearwood, C.; Fu, Y.Q.; Yu, L.; Khor, K.A. Spark plasma sintering of TiNi nano-powder. *Scr. Mater.* **2005**, *52*, 455–460. [CrossRef]
9. Shi, Z.; Wang, J.; Wang, Z.; Qiao, Y.; Xiong, T.; Zheng, Y. Cavitation Erosion and Jet Impingement Erosion Behavior of the NiTi Coating Produced by Air Plasma Spraying. *Coatings* **2018**, *8*, 346. [CrossRef]
10. Feng, Y.; Du, Z.; Hu, Z. Effect of Ni Addition on the Corrosion Resistance of NiTi Alloy Coatings on AISI 316L Substrate Prepared by Laser Cladding. *Coatings* **2021**, *11*, 1139. [CrossRef]
11. Salvetr, P.; Dlouhý, J.; Školáková, A.; Průša, F.; Novák, P.; Karlík, M.; Haušild, P. Influence of Heat Treatment on Microstructure and Properties of NiTi46 Alloy Consolidated by Spark Plasma Sintering. *Materials* **2019**, *12*, 4075. [CrossRef] [PubMed]
12. Samal, S.; Tyc, O.; Cizek, J.; Klecka, J.; Lukáč, F.; Molnárová, O.; de Prado, E.; Weiss, Z.; Kopeček, J.; Heller, L.; et al. Fabrication of Thermal Plasma Sprayed NiTi Coatings Possessing Functional Properties. *Coatings* **2021**, *11*, 610. [CrossRef]
13. Tomastik, J.; Ctvrtlik, R.; Drab, M.; Manak, J. On the Importance of Combined Scratch/Acoustic Emission Test Evaluation: SiC and SiCN Thin Films Case Study. *Coatings* **2018**, *8*, 196. [CrossRef]
14. Sewak, R.; Dey, C.C. Martenitic phase transformation in NiTi. *Sci. Rep.* **2019**, *9*, 13500. [CrossRef] [PubMed]
15. Xu, J.; Bao, L.; Liu, A.; Jin, X.; Tong, Y.; Luo, J.; Zhong, Z.; Zheng, Y. Microstructure, mechanical properties and superelasticity of biomedical porous NiTi alloy prepared by microwave sintering. *Mater. Sci. Eng. C* **2015**, *46*, 387–393. [CrossRef]
16. Velmurugan, C.; Senthilkumar, V.; Biswas, K.; Yadav, S. Densification and microstructural evolution of spark plasma sintered NiTi shape memory alloy. *Adv. Powder Technol.* **2018**, *29*, 2456–2462. [CrossRef]
17. Yadav, K.C.; Verma, M. Review of tribology (friction, wear and lubrication) study on titanium and its alloy surfaces. *Int. J. Rec. Adv. Eng. Technol.* **2016**, *2347*, 58–63.
18. Yang, R.; Ma, W.; Duan, C.; Yang, Z.; Zhang, Y.; Wang, T.; Wang, Q. Tribologically induced amorphization in the subsurface of aged Ni-rich TiNi alloy during dry sliding. *Intermetallics* **2019**, *113*, 106574. [CrossRef]
19. Wang, Y.; Xu, R.; Hu, S.; Tu, F.; Jin, W. Research combining experiment and FEM analysis on sliding wear behaviors and mechanisms of TiNi alloy. *Wear* **2017**, *386–387*, 218–222. [CrossRef]
20. Rominiyi, A.L.; Shongwe, M.B.; Ogunmuyiwa, E.N.; Babalola, B.J.; Lepele, P.F.; Olubambi, P.A. Effect of nickel addition on densification, microstructure and wear behaviour of spark plasma sintered CP-titanium. *Mater. Chem. Phys.* **2020**, *240*, 122130.
21. Samal, S.; Molnárová, O.; Průša, F.; Kopeček, J.; Heller, L.; Šittner, P.; Škodová, M.; Abate, L.; Blanco, I. Net-Shape NiTi Shape Memory Alloy by Spark Plasma Sintering Method. *Appl. Sci.* **2021**, *11*, 1802. [CrossRef]
22. Ctvrtlik, R.; Tomastik, J.; Vaclavek, L.; Beake, B.D.; Harris, A.J.; Martin, A.S.; Hanak, M.; Abrham, P. High-Resolution Acoustic Emission Monitoring in Nanomechanics. *JOM* **2019**, *71*, 3358–3367. [CrossRef]
23. Lukás, P.; Sittner, P.; Neov, D.; Novák, V.; Lugovoy, D.; Tovar, M. R-Phase Phenomena in Neutron Diffraction Investigations of Thermomechanically Loaded NiTi Polycrystals. *Mater. Sci. Forum Vol.* **2002**, *404–407*, 835–840. [CrossRef]
24. Ling, H.C.; Roy, K. Stress-Induced Shape Changes and Shape Memory in the R and Martensite Transformations in Equiatomic NiTi. *Metall Mater. Trans. A* **1981**, *12*, 2101–2111. [CrossRef]
25. Salvetr, P.; Kubatík, T.F.; Pignol, D.; Novák, P. Fabrication of Ni-Ti Alloy by Self-Propagating High-Temperature Synthesis and Spark Plasma Sintering Technique. *Metall. Mater. Trans. B* **2017**, *48*, 772–778. [CrossRef]
26. Ni, W.; Cheng, Y.T.; Lukitsch, M.J.; Weiner, A.M.; Lev, L.C.; Grummon, D.S. Effects of the ratio of hardness to Young's modulus on the friction and wear behavior of bilayer coatings. *Appl. Phys. Lett.* **2004**, *85*, 4028–4030. [CrossRef]
27. Pintaude, G. Introduction of the Ratio of the Hardness to the Reduced Elastic Modulus for Abrasion. In *Tribology-Fundamentals and Advancements*; Gegner, J., Ed.; IntechOpen: London, UK, 2013.
28. Nishida, M.; Wayman, C.M.; Honma, T. Precipitation processes in near-equiatomic TiNi shape memory alloys. *Metall. Trans. A* **1986**, *17*, 1505–1515. [CrossRef]
29. Adharapurapu, R.R.; Jiang, F.; Vecchio, K.S. Aging effects on hardness and dynamic compressive behavior of Ti–55Ni (at.%) alloy. *Mater. Sci. Eng. A* **2010**, *527*, 1665–1676. [CrossRef]
30. Archard, J.F. Contact and rubbing of flat surfaces. *J. Appl. Phys.* **1953**, *24*, 981–988. [CrossRef]
31. Samal, S. Thermal plasma technology: The prospective future in material processing. *J. Clean. Prod.* **2017**, *142*, 3131–3150. [CrossRef]
32. Tomastik, J.; Ctvrtlik, R.; Ingr, T.; Manak, J.; Opletalova, A. Effect of Nitrogen Doping and Temperature on Mechanical Durability of Silicon Carbide Thin Films. *Sci. Rep.* **2018**, *8*, 10428. [CrossRef] [PubMed]

33. Saedi, S.; Turabi, A.S.; Taheri Andani, M.; Haberland, C.; Karaca, H.; Elahinia, M. The influence of heat treatment on the thermomechanical response of Ni-rich NiTi alloys manufactured by selective laser melting. *J. Alloys Compd.* **2016**, *677*, 204–210. [CrossRef]

34. Hu, Z.-Y.; Zhang, Z.-H.; Cheng, X.-W.; Wang, F.-C.; Zhang, Y.-F.; Li, S.-L. A review of multi-physical fields induced phenomena and effects in spark plasma sintering: Fundamentals and applications. *Mater. Des.* **2020**, *191*, 108662. [CrossRef]

35. Cai, W.; Men, X.L.; Zhao, L.C. Recent development of TiNi-based shape memory alloys. *Solid State Mater. Sci.* **2005**, *9*, 296–302. [CrossRef]

36. de Araújo, C.J.; da Silva, N.J.; da Silva, M.M.; Gonzalez, C.H. A comparative study of Ni–Ti and Ni–Ti–Cu shape memory alloy processed by plasma melting and injection molding. *Mater. Des.* **2011**, *32*, 4925–4930. [CrossRef]

37. Gonzalez, C.H.; Oliveira, C.A.N.; Pina, E.A.C.; Filho, S.L.U.; Filho, O.O.A.; de Araújo, C.J. Heat treatments and thermomechanical cycling influences on the R-phase in Ti–Ni shape memory alloys. *Mater. Res.* **2010**, *13*, 325–331. [CrossRef]

38. Pharr, G.M.; Oliver, W.C.; Cook, R.F.; Kirchner, P.D.; Kroll, M.C.; Dinger, T.R.; Clarke, D.R. Electrical resistance of metallic contacts on silicon and germanium during indentation. *J. Mater. Res.* **1992**, *7*, 961–972. [CrossRef]

39. Tsui, T.Y.; Pharr, G.M.; Oliver, W.C.; Chung, Y.W.; Cutiongco, E.C.; Bhatia, C.S.; White, R.L.; Rhoades, R.L.; Gorbatkin, S.M. Nanoindentation and nano scratching of hard coating materials for magnetic disks. *Mater. Sci. Eng.* **1995**, *356*, 767–772.

40. Beake, B.D.; Isern, L.; Bhattacharyya, D.; Endrino, J.L.; Lawson, K.; Walker, T. Nano- and micro-scale impact testing of zirconia, alumina and zirconia-alumina duplex optical coatings on glass. *Wear* **2020**, *462–463*, 203499. [CrossRef]

41. Arciniegas, A.; Casals, J.; Manero Pena, J.; Gil, F.J. Study of hardness and wear behaviour of NiTi shape memory alloys. *J. Alloy. Compo.* **2008**, *460*, 213–219. [CrossRef]

42. Burnett, P.J.; Rickerby, D.S. The relationship between hardness and scratch adhesion. *Thin Solid Films* **1987**, *154*, 403–416. [CrossRef]

43. Li, D.Y.; Liu, R. The mechanism responsible for high wear resistance of pseudo-elastic TiNi alloy-a novel tribo-material. *Wear* **1999**, *225–229*, 777–783. [CrossRef]

44. Neupane, R.; Farhat, Z. Wear and Dent Resistance of Superelastic TiNi Alloy. *Wear* **2013**, *301*, 682–687. [CrossRef]